Overcoming excessive numerical dissipation in SPH modeling of water waves

V. Zago[a,*], L. J. Schulze[a,b], G. Bilotta[c], N. Almashan[d], R. A. Dalrymple[a]

[a] *Dept. of Civil and Environmental Engineering, Northwestern University, 2145 Sheridan Road, Evanston, IL 60208, USA*
[b] *Institute for Computational Mechanics, Technical University of Munich, Garching bei München, Germany*
[c] *Osservatorio Etneo, Istituto Nazionale di Geofisica e Vulcanologia, Catania, Italy*
[d] *Civil Engineering Department, College of Engineering and Petroleum, Kuwait University*

Abstract

Excessive nonphysical energy dissipation is a problem in Smoothed Particle Hydrodynamics (SPH) when modeling free surface waves, resulting in a significant decrease in wave amplitude within a few wavelengths for progressive waves. This dissipation poses a limitation to the physical scale of SPH applications involving water wave propagation. Some prior solutions to this wave decay problem rely on elaborate schemes, which require a complex, or non-straightforward, implementation. Other approaches demand large smoothing lengths that lead to longer simulation times and potential degradation of the results. In this work we present an approach based on a kernel gradient correction. Our scheme is fully 3D and solves the main known drawbacks of kernel gradient corrections, such as instabilities and lack of momentum conservation. The latter is ensured by adopting an averaged correction matrix, so as to conserve reciprocity during particle interactions. We test our model with a standing wave in a basin and a progressive wave train in a wave tank, and in both cases no nonphysical decay occurs. A comparison to an approach based on large smoothing factors shows advantages both in quality of the results and simulation time.

Keywords: WCSPH, wave propagation, coastal engineering, kernel correction,

*Corresponding author
Email address: vito.zago@northwestern.edu (V. Zago)

decay

2021 MSC:

1. Introduction

Water wave propagation constitutes a problem of great importance for a wide range of scientific topics in nearshore physical oceanography and coastal engineering. Numerical simulations are gaining relevance in applications involving wave shoaling, coastal hydrodynamics, or wave-structure interaction [1]. Smoothed Particle Hydrodynamics (SPH) is a meshless Lagrangian method in 2- and 3D that allows a straightforward tracking of free-surfaces, making it a promising method for this purpose [2, 3, 4, 5, 6, 7, 8, 9, 10, 11, 12, 13, 14, 15, 16, 17, 18, 19]. However, basic SPH models can exhibit substantial numerical dissipation when simulating wave propagation, leading to excessive loss of wave energy. Without further remedies, this problem potentially limits the applicability of SPH to small scale water wave problems.

The comprehensive study by Colagrossi *et al.* [3] concludes that basic SPH models are capable of accurately predicting the attenuation process in viscous standing waves. The number of neighbors per particle is the decisive factor, and a minimum amount is needed in order to achieve convergence towards analytical results with refining spatial resolution. The convergence properties were studied for a range of Reynolds numbers, showing that a higher number of neighbors is needed for larger Reynolds numbers. While the choice of the kernel function can improve the results, at least to some extent [3, 4, 14, 18, 10], the simulation of waves with large Reynolds numbers quickly demands an unrealistic amount of computational effort due to the required number of neighbors and spatial resolution. Furthermore, the large smoothing length causes additional layers of particles to be in the free-surface region, where particle supports are incomplete, and may result in a severe particle disordering at the free-surface.

Numerous studies report a range of schemes that relax the requirements discussed by Colagrossi *et al.* [3]. Chang *et al.* [14] employ a sixth-order kernel

with a large smoothing length. This approach is simple and provides accurate results. However, the required number of neighbors per particle calls for a large computational effort, which increases significantly in 3D. The inclusion in the conservation of mass equation of density diffusion terms that stabilize the pressure field, as in the δ-SPH formulation [20, 21], has also been shown to improve the conservation of energy, but large kernel supports are still needed to obtain good levels of conservation [5, 22]. Riemann solvers [6, 16, 18] also result in an improvement of wave propagation with SPH, but those often involve a complex implementation and do not account for any viscous terms without special treatment.

Kernel gradient correction (KGC) is another approach; Guilcher [6], Wen [15] and Gao [16] incorporated various forms of KGC into SPH models. These corrections are based on the original proposition by Randles and Libersky [23] and Johnson and Beissel [24], which also appears in the Corrective Smoothed Particle Method (CSPM) by Chen and Beraun [25]. The latter was proposed as a method for addressing tensile instability. The correction technique adopted in KGC stems from the Taylor expansion of the SPH interpolation and is known to enhance the consistency of the SPH approximation of the kernel gradient [26]. As a result, KGC significantly improves the simulation of wave propagation without requiring any extensive increase of the smoothing length [15]. But KGC schemes also present some known drawbacks, one of which is the lack of momentum conservation [20], resulting from the fact that the coefficients correcting the kernel gradients are applied to individual particles, instead of particle pairs. This approach does not guarantee symmetric interactions during force computations, which can result in loss or gain of wave momentum and energy. A second problem of KGC arises when the correction coefficients are applied to certain geometrical particle configurations, such as free-surfaces, which can generate significant errors or instabilities in the simulations [27].

In this work, we will first show the numerical dissipation associated with standard SPH when simulating progressive wave trains and standing waves in a basin. We then present a new approach to KGC where coefficients are computed

considering particle pairs, ensuring that the particle interactions are symmetric. A strategy to avoid the instabilities illustrated by Xiao *et al.* [27] is also presented. After a validation of the new numerical scheme, we show the simulation of progressive waves in a long wave tank, where a wavetrain thirty wave lengths long is considered. The results suggest that the proposed method can accurately predict water wave propagation, while ensuring good stability and simulation performance.

2. The Standard SPH scheme: SSPH

In our 3D SPH scheme the domain is initially discretized by means of a set of regularly spaced particles, with the inter-particle distance denoted as Δp. We indicate with $\mathbf{x}_i$ the position of a generic particle i, where $\mathbf{x} = (x, y, z)^T$, and $\mathbf{u}_i$ the velocity of the particle. Following [28], we denote the SPH approximation of a generic function $f(\mathbf{x})$ evaluated at a particle i as:

$$f(\mathbf{x}_i) = \sum_j f(\mathbf{x}_j) W(r_{ij}, h) V_j. \tag{1}$$

Here, V_j is the volume of a particle j, positioned at $\mathbf{x}_j$, and W indicates the SPH smoothing kernel. The distance from particle j to particle i is denoted by r_{ij} and the SPH smoothing length is denoted by h. The latter can be expressed in terms of inter-particle spacing Δp by writing $h = \alpha_s \Delta p$, where α_s is the smoothing factor. For computational convenience, W is defined on a compact support and hence the summation over j is limited to the particles within the support. We refer to these particles as neighbors. In 3D the support is a sphere centered at x_i with a radius taken as a multiple of h. This radius is typically referred to as the influence radius.

We now specify the details of the SPH scheme that we will use as a reference model to illustrate the problem of numerical damping. For convenience, we will denote this standard SPH scheme as SSPH. We use the fifth order Wendland smoothing kernel [29], which has been observed to be beneficial for free-surface simulations [4]. This kernel has a smoothing radius $2h$, and, in three dimensions,

is defined as:

$$W(r,h) = \begin{cases} \dfrac{21}{16\pi h^3}\left(1-\dfrac{q}{2}\right)^4(1+2q) & \text{if} \quad 0 \le q \le 2 \\ 0 & \text{if} \quad q > 2, \end{cases} \tag{2}$$

where $q = r/h$. We will use $\alpha_s = 1.3$, which is a commonly adopted value for the smoothing factor [28, 30].

Considering the radial symmetry of the smoothing kernel, we can define a function $F(r,h)$, such that

$$F(r,h) = \frac{1}{r}\frac{\partial W(r,h)}{\partial r} \tag{3}$$

has an analytical expression. For the Wendland kernel it is:

$$F(r,h) = \begin{cases} \dfrac{105}{128\pi h^5}(q-2)^3 & \text{if} \quad 0 \le q \le 2 \\ 0 & \text{if} \quad q > 2. \end{cases} \tag{4}$$

This expression implicitly accounts for divisions by r in many formulas involving $\nabla W(\cdot, h)$ that would otherwise cause instabilities for spatially close particles.

Our model is based on the three-dimensional Navier–Stokes equation for mass and momentum conservation. The discretized equation for mass conservation is written as

$$\frac{D\rho_i}{Dt} = \sum_j \mathbf{u}_{ij} \cdot \mathbf{x}_{ij} F_{ij} m_j + \xi h c_0 \sum_j \Psi_{ij} F_{ij} m_j. \tag{5}$$

Here, the second term on the right hand side is the density diffusion contribution, presented in [31] and modified by Equation 3, giving:

$$\Psi_{ij} = \begin{cases} 2\left(\dfrac{\rho_j}{\rho_i} - 1\right) & \text{if} \quad \dfrac{|P_i - P_j|}{\rho_i g |z_i - z_j|} > 1 \\ 0 & \text{otherwise.} \end{cases} \tag{6}$$

ξ is the density diffusion coefficient [31], that we take equal to 0.1, and c_0 is the speed of sound in the fluid domain. This diffusive term improves the pressure field and the stability of the simulations, while requiring a limited computational load [15]. A more recent density diffusion term was proposed by Antuono *et al.* [32], adopted in the δ-SPH formulation [20], constituting an improvement of

Equation 6. Among the enhancements, the new term solves some consistency issues that arise at the free surface for stationary hydrostatic pressure fields [21], at the expense of higher computational load. Because of the dynamic nature of wave propagation problems, the term in Equation 6 is able to provide enough stability to the simulations, constituting a good compromise with computational time. However, as described in [21] the adopted diffusion term is independent on the SPH scheme and transition to a different density diffusion term is possible whereas desired.

The equations for momentum conservation are

$$\frac{D\mathbf{u}_i}{Dt} = \sum_j \left(\frac{P_i}{\rho_i^2} + \frac{P_j}{\rho_j^2} + \Pi_{ij} \right) \mathbf{x}_{ij} F_{ij} m_j + \mathbf{g}, \tag{7}$$

where $\mathbf{g} = (0, 0, -9.81)^T$ is the gravity vector and Π_{ij} is the artificial viscosity term, defined as [28]

$$\Pi_{ij} = \begin{cases} -\dfrac{\alpha\, h\, c_0}{\rho_j} \left(\dfrac{\mathbf{u}_{ij} \cdot \mathbf{x}_{ij}}{|\mathbf{x}_{ij}|^2 + \epsilon h^2} \right) & \text{if} \quad (\mathbf{u}_{ij} \cdot \mathbf{x}_{ij}) > 1 \\ 0 & \text{otherwise.} \end{cases} \tag{8}$$

Here, ϵ is a constant set to 0.01, introduced to prevent a singularity when $|\mathbf{x}_{ij}|^2$ is very small [28], and α is the artificial viscosity coefficient. In order to reproduce an equivalent kinematic viscosity, ν, we use the relationship [28]

$$\alpha = \frac{10\,\nu}{h\, c_0}. \tag{9}$$

The pressure P is obtained from the density using Cole's [33] equation of state:

$$P(\rho) = c_0^2 \frac{\rho_0}{\gamma} \left[\left(\frac{\rho}{\rho_0} \right)^{\gamma} - 1 \right]. \tag{10}$$

Here, ρ_0 is the reference density of the fluid and γ is the polytropic constant, that we take equal to 7.

We adopt a second order predictor-corrector integration scheme described by the following steps:

1. Compute accelerations and density derivatives at instant n:
   a) $\mathbf{a}^{(n)} = \mathbf{a}(\mathbf{x}^{(n)}, \mathbf{u}^{(n)}, \rho^{(n)})$,

b) $\dot{\rho}^{(n)} = \dot{\rho}(\mathbf{x}^{(n)}, \mathbf{u}^{(n)}, \rho^{(n)})$,

2. Compute half-step intermediate positions, velocities and densities:

a) $\mathbf{x}^{(n\star)} = \mathbf{x}^{(n)} + \mathbf{u}^{(n)} \frac{\Delta t}{2}$,

b) $\mathbf{u}^{(n\star)} = \mathbf{u}^{(n)} + \mathbf{a}^{(n)} \frac{\Delta t}{2}$,

c) $\rho^{(n\star)} = \rho^{(n)} + \dot{\rho}^{(n)} \frac{\Delta t}{2}$,

3. Compute corrected accelerations and density derivatives:

a) $\mathbf{a}^{(n\star)} = \mathbf{a}(\mathbf{x}^{(n\star)}, \mathbf{u}^{(n\star)}, \rho^{(n\star)})$,

b) $\dot{\rho}^{(n\star)} = \dot{\rho}(\mathbf{x}^{(n\star)}, \mathbf{u}^{(n\star)}, \rho^{(n\star)})$,

4. Compute new positions, velocities and densities:

a) $\mathbf{x}^{(n+1)} = \mathbf{x}^{(n)} + (\mathbf{u}^{(n)} + \mathbf{a}^{(n\star)} \frac{\Delta t}{2}) \Delta t$,

b) $\mathbf{u}^{(n+1)} = \mathbf{u}^{(n)} + \mathbf{a}^{(n\star)} \Delta t$,

c) $\rho^{(n+1)} = \rho^{(n)} + \dot{\rho}^{(n\star)} \Delta t$.

The time step Δt is computed for each particle i and is required to fulfill CFL-like stability conditions determined by the acceleration magnitude and speed of sound:

$$\Delta t_i \leq \min \left\{ 0.3 \sqrt{\frac{h}{||a_i||}}, 0.3 \frac{h}{c_0} \right\}. \tag{11}$$

The resulting overall time step for the model is chosen as the minimum particle time step. Following the approach of Monaghan [28], the value of c_0 is taken to be lower than the physical speed of sound to avoid very small time steps. For free surface flow problems, to avoid a large fluid compressibility, the value c_0 is typically chosen one order of magnitude above the Torricelli Theorem velocity, $c_h = \sqrt{2gd}$ (with d being the tallest fluid column in the simulation domain) or the highest particle velocity, u_{max}, expected in the problem under consideration, if $u_{max} > c_h$. In our formulation we choose

$$c_0 = 20 \max \{c_h, u_{max}\}. \tag{12}$$

All of the schemes shown in this paper are 3D and are implemented in the open source code GPUSPH [34]. Computations are performed on GPUs in single numerical precision and we incorporate some accuracy improvements, like relative density and position [35].

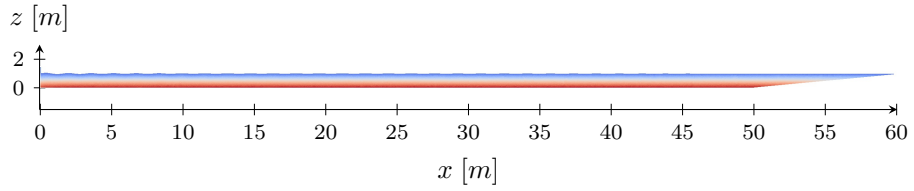

(a)

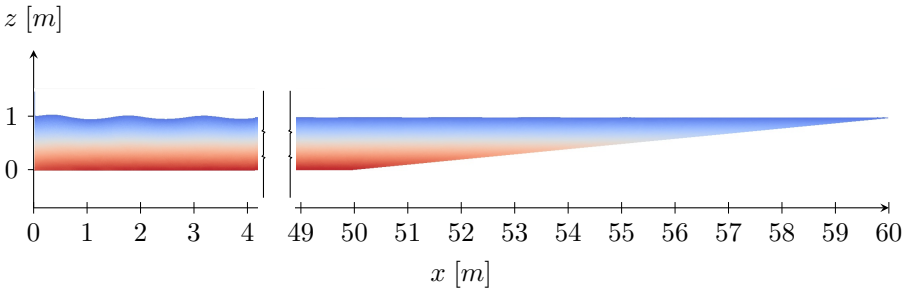

(b)

Figure 1: x–z view of the numerical wave tank (NWT) where waves with height $H = 0.08$m and wavelength $\lambda = 1.5$m are being generated in a depth of 1 m. Colors relate to the pressure experienced by the SPH particles. Figure (a) displays the entire NWT, whereas Figure (b) highlights details of the beginning and end of the NWT.

3. Wave decay in SSPH

For the simulation of progressive gravity waves, we consider the three-dimensional numerical wave tank (NWT) shown in Figure 1. The tank has a flat region of length $l_f = 50$m with a still water level of $d = 1$m, and it terminates with a 10m long sloping region (10% slope) to reduce wave reflection from the end. The wavemaker is modeled with Lennard-Jones particles and the tank bottom with Lennard-Jones planes [13]. Periodic boundary conditions are imposed on the side walls, and the domain has a width of $8h$ rounded up to the next multiple of Δp. The simulated waves have a height of $H = 0.08$m (peak-to-peak amplitude) and are generated by means of a piston wavemaker. We use an SPH resolution of 128 particles per meter ($\Delta p = 1/128$ m). The density of a particle is initialized according to its hydrostatic pressure, $\rho_i(t_0) = \rho(P(z_i(t_0)))$, and the mass is

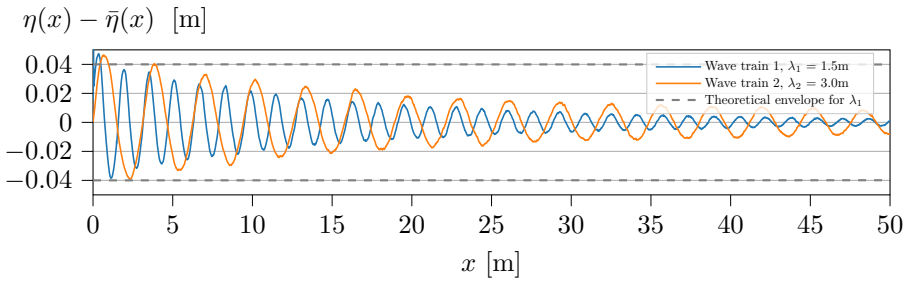

(a)

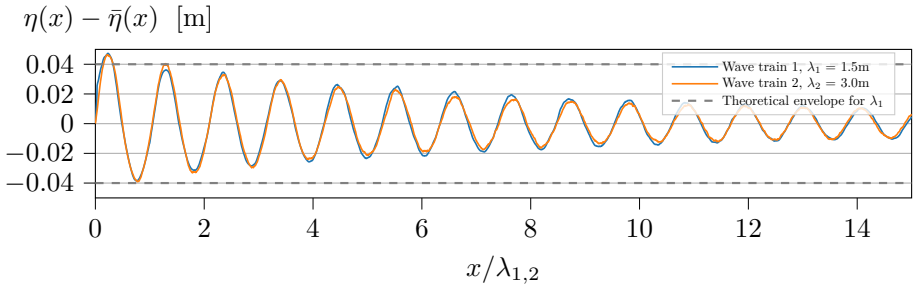

(b)

Figure 2: Surface elevation in the NWT for two wave trains with different wavelengths, simulated with the SSPH. Figure (a) displays surface elevation plotted against distance down the tank. Figure (b) displays surface elevation plotted against the distance normalized by the wavelength of the respective wavetrain; the decay depends on the number of wavelengths that the wave has travelled. The theoretical envelope is shown only for λ_1 as in this plot it would be indistinguishable from that of λ_2.

taken as $m_i = \rho_i(t_0)\Delta p^3$. The artificial viscosity is set according to Equation 9, and a value of $\nu = 10^{-6}\text{m}^2/\text{s}$ is chosen. The simulation is run up to a time t_{end}, necessary for the wave train to reach the end of the flat region.

Two tests were simulated for progressive wave trains using SSPH for waves with wavelengths of $\lambda_1 = 1.5$m and $\lambda_2 = 3$m, corresponding to a wave periods of 0.98s and 1.407s respectively. Figure 2 shows the free-surface elevation, denoted with $\eta(x)$, at the time t_{end}. A de-trending has been performed by subtracting lower frequency fluctuations of the mean water level along the tank, defined as $\bar{\eta}(x)$. This allows us to isolate and better analyze the amplitude of the

progressive waves. These low-frequency oscillations are a seiche motion triggered at the startup of the simulation by the rearrangement of the SPH particles and the startup of the wave paddle. The profile $\bar{\eta}(x)$ is obtained from the free-surface elevations by filtering out the propagating waves. This filtering is performed by means of a moving average, using a one-wavelength-wide spatial window.

The water surface elevation for a progressive wave in a viscous medium can be obtained from linear wave theory as [36]:

$$\eta(x) = \frac{H}{2} e^{-\frac{4\nu k^3 x}{\omega}} \cos(kx - \omega t), \tag{13}$$

where $\omega = 2\pi/T$ is the angular frequency of the wave and $k = 2\pi/\lambda$ is the wave number. In Figure 2 (a), we compare the simulated results with the analytical solution for each test. The dashed lines in figure mark the envelope of the analytical solution along the wave tank. While the decay predicted by the theoretical model is not appreciable within the length of the tank, an excessive decay can be observed in the simulated solutions, with the shorter waves ($\lambda =$ 1.5m) decaying faster with distance. We note from these simulations that, unlike the viscous decay, the spurious decay has a linear dependence on the wave number, attenuating the amplitude of a propagating wave according to the number of wavelengths traveled, independent of the value of λ. By non-dimensionalizing the distance traveled by each wavetrain by its wavelength, we can directly see a correspondence between the decay rate of the two wave trains (Figure 2b). Therefore, in the rest of this work, all distances will be non-dimensionalized by wave length.

The energy in water waves consists of potential and kinetic energy. Linear wave theory shows that the these energies have equal magnitude and they are proportional to the square of the wave height. For a standing wave, the energy will oscillate between pure potential to purely kinetic during the motion. Here we measure the kinetic energy in a standing wave in a basin over time. This approach has been used in other works [19, 3], making a comparison with other results in the literature possible. We use the same settings adopted in [5], except

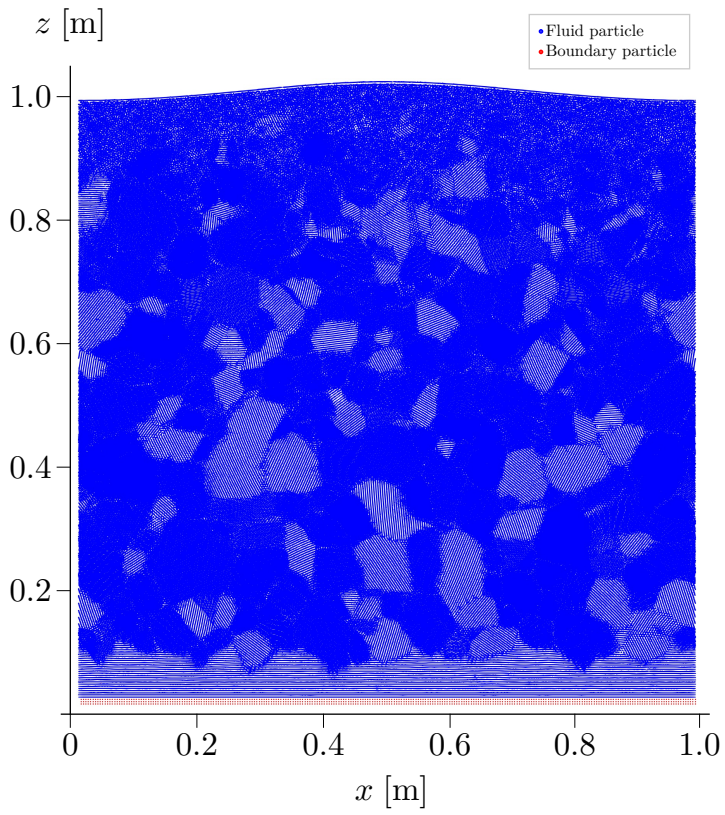

Figure 3: x–z view of the domain for the simulation of the standing wave. Light blue patterns are optical effects resulting from particle alignment in the y direction.

that our example is in 3D, not 2D. The domain has a square shape in the x and z directions, with a side of $d = 1$m (see Figure 3), and we assign it a thickness of $6h$ in the y direction. Periodic boundary conditions are used in the x and y directions. As in the NWT problem, the density and the mass of the particles are initialized hydrostatically. A standing gravity wave of height H and wavelength equal to the basin length is generated by means of an initial velocity potential field, described as

$$\phi(x, z, t) = \phi_0(x, z) \cos(\omega t), \tag{14}$$

with

$$\phi_0(x, z) = -\epsilon \frac{dg}{2\omega} \frac{\cosh[k(z + d)]}{\cosh(kd)} \cos(kx), \tag{15}$$

where $\epsilon = H/d$. The relationship between the wave number k and the wave/seiching frequency ω is obtained from the dispersion relation

$$\omega^2 = gk \tanh(kd). \tag{16}$$

where g is the modulus of the gravity vector, equal to 9.81m/s^2. For the setup described above, we obtain $\omega = 7.85$rad/s, that corresponds to a wave period of 0.8s. The theoretical evolution of the kinetic energy for a standing wave is an oscillation with frequency 2ω, decaying exponentially at a rate determined by the viscosity and the wave number. An analytical expression for the kinetic energy in the basin is [5]:

$$E_{kin}(t) = \epsilon^2 \rho_0 \, g \, b \frac{\lambda d^2}{32} e^{-4\nu k^2 t} \left[1 + \cos(2\omega t)\right], \tag{17}$$

where b is the thickness of the tank in the y direction and ρ is included to make the equation dimensionally correct. In the case of water, the decay is negligible over a short period of time.

From the SPH point of view, we use a $\Delta p = 1/256$m and a smoothing factor $\alpha_s = 1.3$. Figure 4a shows the kinetic energy for the standing wave with $H = 1/16 = 0.0625$m), simulated using SSPH (Section 2). The kinetic energy of the standing wave is indicated by the periodic oscillations, which are decaying

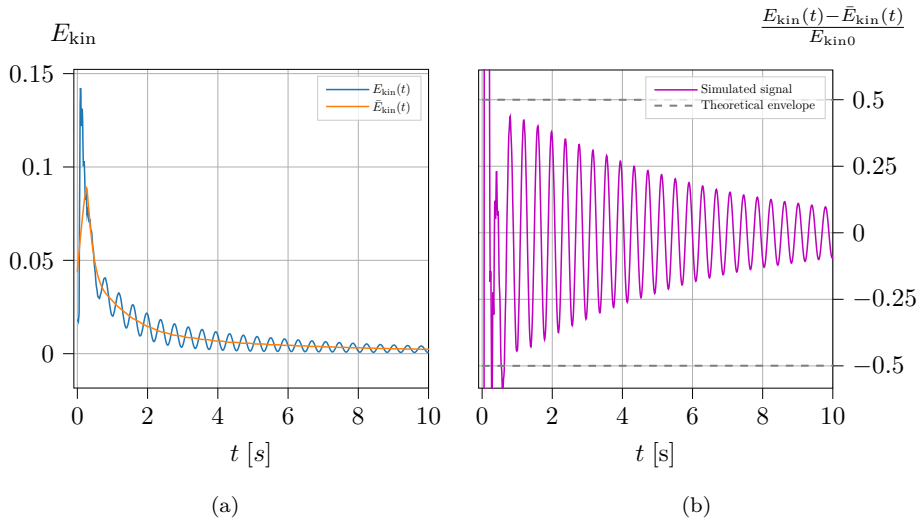

Figure 4: Temporal evolution of kinetic energy for the standing wave problem simulated with SSPH formulation. Figure (a) displays the instantaneous kinetic energy and its one-period-wide moving average. Figure (b) displays the postprocessed kinetic energy. Dashed lines show the envelope of the analytical solution, Equation 17.

rapidly over time. A slower shifting of the curve can be observed that prevents the energy oscillations from reaching zero at the instants when the wave has zero velocity (trough and crest positions). This additional kinetic energy comes mainly from particles mixing up when re-settling from their initial configuration [37]. Hereafter, this shifting will be filtered out in order to allow a better evaluation of the amplitude of the wave associated oscillations. An approach based on a one-period-wide moving average is used also in this case. Figure 4b shows the filtered trend, and the decay is compared to the analytical solution (dashed lines) obtained using Equation 17. The irregularities present on the first few periods are due to the limits of the filtering process. During the initial phase, the energy coming from particle mixing varies with a frequency comparable with that of the wave-associated oscillations, and therefore the dynamics due to the particle mixing cannot be filtered out using the moving average approach. A normalization of the energy by its initial value is also performed, so that the

initial energy oscillation has unit amplitude and is centered on zero, allowing an easier reading of the percentage of decayed energy, and accounting for different thicknesses of the domain due to differing smoothing factors.

4. Corrected formulation

In accordance with the consistency condition on the smoothing factor [38]

$$\alpha_s = h/\Delta p \to \infty, \tag{18}$$

the study by Colagrossi *et al.* [3] shows that larger values of α_s can reduce the amount of numerical dissipation of gravity waves. This benefit comes at the expense of a higher computational cost and simulation time. In fact, most of the computation of a SPH simulation lies in the particle-particle interactions (i.e. summations over the neighbors), where the number of interactions grows with the cube of α_s in the three-dimensional case. For this reason, typical suggested values of α_s range between 1.2 and 1.5 [39], while Colagrossi *et al.* [3] shows that acceptable decay rates for high Reynolds number simulations are obtained for values of α_s greater than 3, implying prohibitive simulation times.

Alternatively we can improve the particle approximation without having large α_s by using a kernel gradient correction [6, 39, 40].

4.1. Standard kernel gradient correction

Kernel gradient correction (KGC) is a technique that is designed to compensate for the error introduced in the SPH approximation of a gradient as a result of discretizing the domain with a finite number of particles (Appendix A).

A KGC is obtained as a linear mapping of the kernel gradient by a corrective matrix. For each particle at location $\mathbf{x}_i = (x_i, y_i, z_i)^T$, the matrix

$$\mathbf{A}_i = \sum_j \nabla W_{ij} \otimes (\mathbf{x}_j - \mathbf{x}_i) V_j = \sum_j \begin{pmatrix} x_{ij}\frac{\partial W_{ij}}{\partial x} & y_{ij}\frac{\partial W_{ij}}{\partial x} & z_{ij}\frac{\partial W_{ij}}{\partial x} \\ x_{ij}\frac{\partial W_{ij}}{\partial y} & y_{ij}\frac{\partial W_{ij}}{\partial y} & z_{ij}\frac{\partial W_{ij}}{\partial y} \\ x_{ij}\frac{\partial W_{ij}}{\partial z} & y_{ij}\frac{\partial W_{ij}}{\partial z} & z_{ij}\frac{\partial W_{ij}}{\partial z} \end{pmatrix} V_j \tag{19}$$

is computed, where $x_{ij} = x_j - x_i$, and similarly for y_{ij} and z_{ij}. See Appendix A for details. From this matrix we define the correction matrices as $\mathbf{B}_i = \mathbf{A}_i^{-1}$, so that the corrected kernel gradient can be written as

$$\tilde{\nabla} W_{ij} = \mathbf{B}_i \nabla W_{ij}. \tag{20}$$

These coefficients are calculated before the computation of the derivatives, which are Steps 1 and 3 of the integration scheme shown in Section 2.

4.2. Reduced correction scheme, CSPH

Typical corrective schemes apply the kernel gradient correction to both the equations of mass and momentum conservation, but the conservation of energy is most directly related to the momentum equation [39]. We therefore limit the correction to the latter, as otherwise some volume conservation issues can occur, especially at low viscosity values.

In our formulation, we adopt the convention expressed by Equation 3, so we rewrite the matrix $\mathbf{A}_i$ as

$$\mathbf{A}_i = \sum_j \begin{pmatrix} x_{ij}^2 & y_{ij}x_{ij} & z_{ij}x_{ij} \\ y_{ij}x_{ij} & y_{ij}^2 & z_{ij}y_{ij} \\ x_{ij}z_{ij} & y_{ij}z_{ij} & z_{ij}^2 \end{pmatrix} F_{ij} V_j. \tag{21}$$

This matrix is symmetric, allowing a smaller computational effort. The order of the matrix is limited to the dimensionality of the problem; therefore the matrix inversion to obtain $\mathbf{B}$ in 3D can be performed analytically. The corrected momentum equation becomes

$$\frac{D\mathbf{u}_i}{Dt} = -\sum_j \left(\frac{P_i}{\rho_i^2} + \frac{P_j}{\rho_j^2} - \Pi_{ij} \right) \mathbf{B}_i \mathbf{x}_{ij} F_{ij} m_j + \mathbf{g}. \tag{22}$$

Henceforth, we will refer to this corrected SPH scheme as CSPH. Let us notice that Taylor-consistent formulations, where the gradient of the pressures is discretized using the difference of the pressures, are typically adopted when using a correction based on the Taylor series (see Appendix A)[41, 39]. However, these formulations do not guarantee conservation of momentum [11] and energy [42]

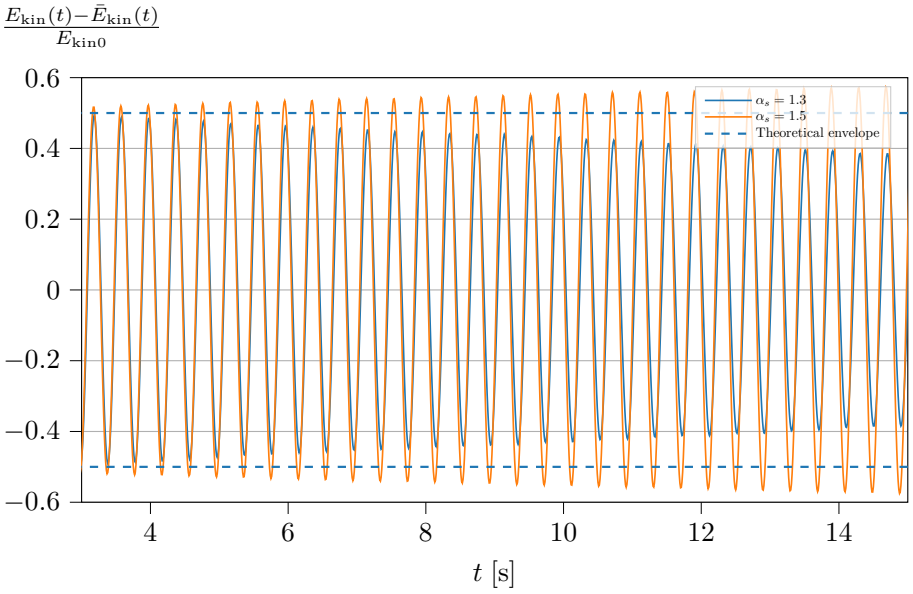

Figure 5: Kinetic energy of a standing wave, simulated with CSPH and two different smoothing factors.

even at continuum level. On the other hand, it has been shown that improved results can be obtained also when applying a KGC to a non Taylor-consistent formulation [15, 39]; considering the scope of this work, we follow this approach since energy conservation is prioritized.

4.3. Symmetrized Correction, CCSPH

Because of the local nature of the correction coefficients, the standard kernel gradient correction (KGC) adopted in CSPH does not guarantee reciprocity in particle-particle interactions [39]. Asymmetric interactions in turn do not guarantee conservation of momentum [20, 43], which can eventually affect the conservation of energy.

Figure 5 shows the trend of kinetic energy for the CSPH formulation introduced in Subsections 4.1 and 4.2 for different values of the smoothing factor, α_s. Even though the kinetic energy is maintained better than in SSPH with $\alpha_s = 1.3$, no convergence is shown towards the analytical solution, with the

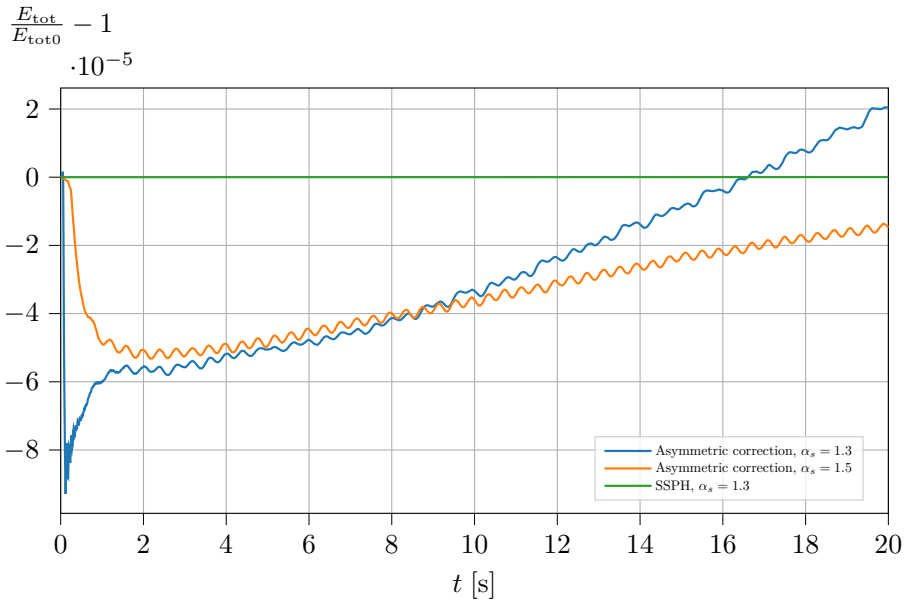

Figure 6: Normalized total energy for SSPH and CSPH at two different smoothing factors.

kinetic energy growing over time for larger α_s. The loss of energy conservation can also be found in the total energy of the system, which is computed as:

$$E_{\text{tot}} = \sum_i \left(\frac{1}{2} m_i \mathbf{u}_i^2 + m_i \mathbf{g} \cdot \mathbf{r}_i + m_i e_i \right), \tag{23}$$

where the terms in parenthesis are the particle kinetic energy, potential energy and internal energy, respectively. The latter is determined from the following equation [35]:

$$\frac{De_i}{Dt} = \frac{1}{2} \sum_j \left(\frac{P_i}{\rho_i^2} + \frac{P_j}{\rho_j^2} + \Pi_{ij} \right) \mathbf{u}_{ij} \mathbf{x}_{ij} F_{ij} m_j. \tag{24}$$

By looking at the trend of the total energy (Figure 6), significant variations are introduced for CSPH. The original SPH formulation shows variations that are three orders of magnitude smaller and are attributable to the machine precision of the calculations.

The conservation issues associated with standard kernel gradient correction can be solved by restoring symmetry in particle-particle interactions. Vila [44]

and Guilcher *et al.* [6] show a case of corrected formulation where interactions are maintained symmetric, presenting an averaged correction with coefficients obtained as

$$\mathbf{B}_{ij} = \frac{1}{2}(\mathbf{A}_i^{-1} + \mathbf{A}_j^{-1}) \tag{25}$$

to be used in Equation 22 in place of $\mathbf{B}_i$. However, we have found that these correction coefficients introduced instabilities in the simulations in presence of a free surface. Figure 7a shows the free surface region for the standing wave problem simulated using the asymmetric correction, as presented in Subsection 4.2, and a resolution of 128 particles per meter. Figure 7b shows the simulation obtained using Equation 25, where the particle distribution in proximity of the free surface is noticeably altered. The correction coefficients that we propose are formulated as

$$\mathbf{B}_{ij} = \left[\frac{1}{2}(\mathbf{A}_i + \mathbf{A}_j)\right]^{-1}. \tag{26}$$

This averaging is more consistent with the geometrical meaning of the matrix $\mathbf{A}$, which is directly related to the configuration of the neighbors in the particle support, and results in a better stability, as shown in Figure 7c. Note that Figure 7 shows a three-dimensional domain with six layers of particles; particle agglomerates are then only a visual effect due to the three dimensional domain. Despite the improved stability of Equation 26, some disordering is introduced in proximity of the free surface with respect to the original non-conservative asymmetric case, with some instabilities arising only at high resolutions, where the single precision adopted for the computations becomes the limiting factor. Instabilities have been encountered at all tested resolutions for the symmetric version of Equation 25. A solution to this problem will be discussed in the next subsection. From a mathematical point of view, the correction matrix with the averaged matrix restores reciprocity in the interactions but introduces an error in the discretized equation. However, the matrices are related to the configuration of the neighboring particles, therefore the error will be smaller as the particles i and j are closer. This condition is consistent with the general idea of keeping the smoothing factor small, so as to limit the size of the particle neigh-

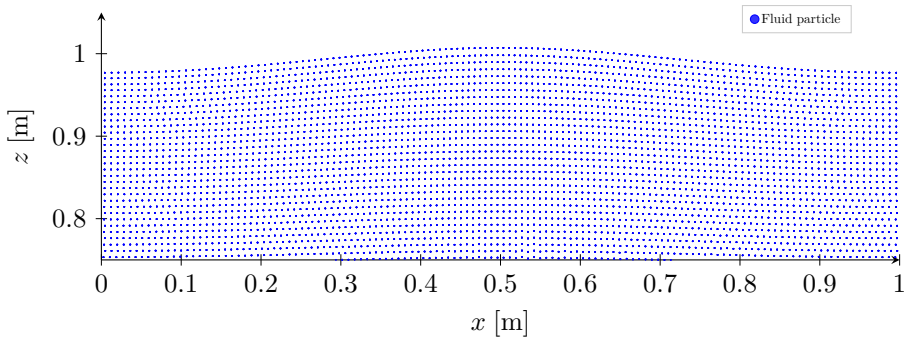

(a)

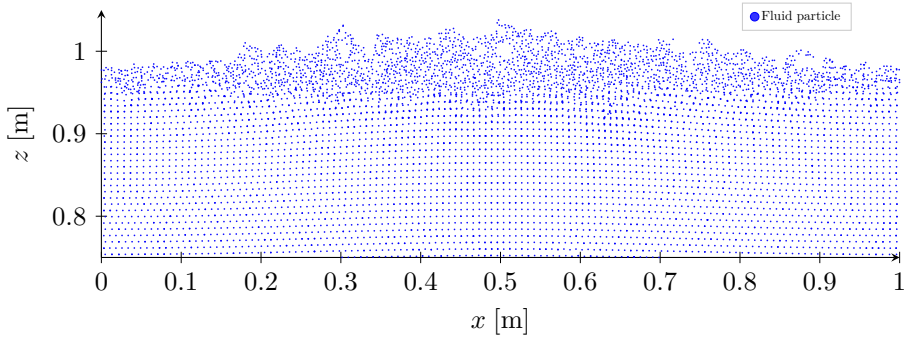

(b)

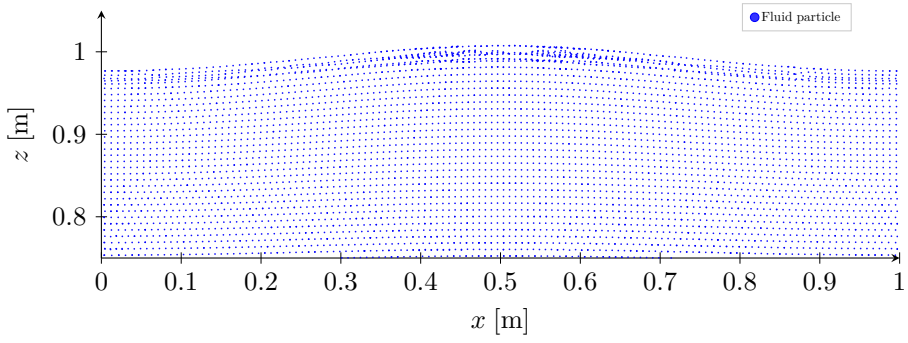

(c)

Figure 7: Particle distributions in the free-surface area at $t = 0.2$s. (a): asymmetric correction; (b): symmetric correction with Equation 25; (c): symmetric correction with Equation 26.

borhood. Preserving momentum conservation is however the main outcome of this symmetric approach. For convenience, we will refer to the newly introduced formulation as CCSPH (Conservative Corrected SPH).

4.3.1. Treatment of free-surface

The use of corrective methods that involve a matrix inversion can cause some known complications when particle supports are incomplete or include distorted particle configurations [39, 27]. These situations typically affect the conditioning of the associated correction matrices [27], leading to instability or loss of accuracy. A special treatment is therefore required for particles with such matrix deficiencies. In the case of gravity waves, a clear example of incomplete support is found at and near the free-surface. Nevertheless, these issues at the free-surface can induce some negative effects on the conservation of the wave energy. Therefore, for the affected particles, we forgo the kernel gradient correction and use an identity matrix ($\mathbf{A} = \mathbf{I}$) in Equation 26 during particle interactions.

The detection of the affected particles with a matrix deficiency is based on the determinant of the matrix. Values of the determinant lower than a certain threshold, $det(\mathbf{A})_{th}$, indicate a matrix deficiency. In order to determine an appropriate threshold, a parameter study was performed, and the quality of the results was analysed by comparing the decay rate of the simulated kinetic energy to the analytical solution provided by Equation 17. The decay rate of the simulated solutions was obtained from an exponential function fitted to the envelope of the kinetic energy signal; the optimal fitting is determined according to the least-squares mean (LSM) approach. We take as a quality index the ratio between the damping exponential coefficient, β, of the fitting function, and the damping exponential coefficient of the analytical solution, $\beta_0 = -4\nu k^2$. Values of the ratio larger than unity indicate a stronger decay than the theoretical one. The solid line in Figure 8 shows the values of β/β_0 obtained for the standing wave problem discretized with 256 particles per meter, and indicates $\det(\mathbf{A})_{th} = 0.6$ as optimal value for the threshold. The choice of this value is reflected on the

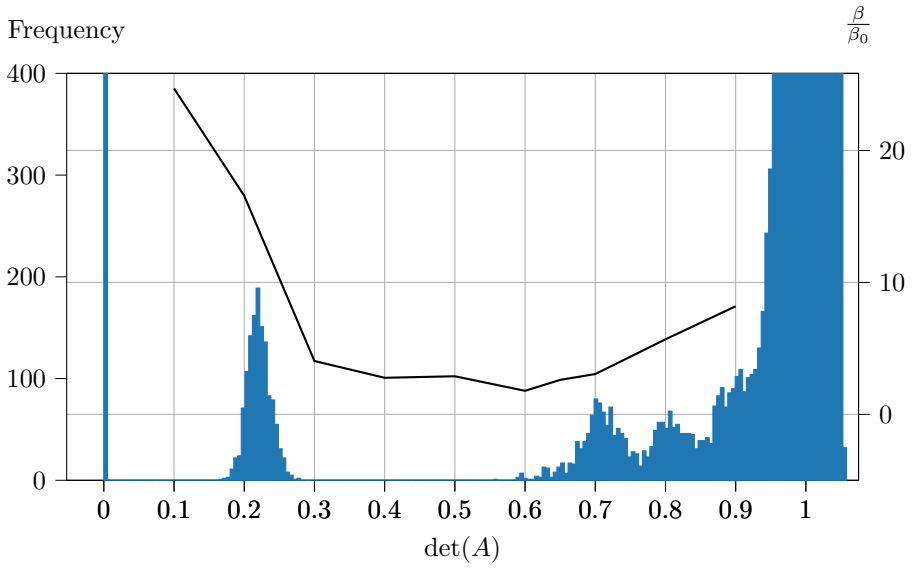

Figure 8: Histogram of the determinant of matrix **A** for fluid particles in the standing wave problem. The plot is truncated in the vertical axis for better visualization. Particle counts on the left. The black line indicates the relative decay ratio as a function of the determinant threshold; right scale.

histogram of the determinants for the entire particle set. The values group up in the histogram mostly in accordance with the location of the particle within the domain (i.e. surface, close to surface, interior); therefore, these histograms do not undergo substantial variations with respect to the simulated problem, once the smoothing function and the dimensionality of the problem are defined. The rightmost set of values in the histogram correspond to particles with full support, while the leftmost are mainly associated with particles on the free-surface. We can say that the optimal threshold should keep the correction on the largest possible amount of particles while discarding all of the particles with a matrix deficiency. This analysis results in our choice of $\det(\mathbf{A})_{th} = 0.6$.

Referring to Figure 7, the optimal threshold additionally restores particle order in the simulations involving averaged matrices with both Equations 25 and 26. The formulation of Equation 26 is anyways preferred as the stability of the simulation would be strongly linked to the presence and the value of the threshold $\det(\mathbf{A})_{th}$.

4.3.2. Treatment of solid boundaries

Fluid particles in proximity of solid boundaries can assume distorted configurations that lead to a degradation of the matrix conditioning [27]. Since boundaries and the neighboring fluid are not actively contributing to the wave propagation, we exclude the kernel gradient correction for boundary particles and fluid particles in their neighborhood. Also in this case, an identity matrix is used for these particles in Equation 26 during particle interactions. The adopted boundary model is therefore not relevant for the design of the corrected scheme. The simulations discussed in this paper adopt a variety of boundary models: a multi-layer model (dynamic boundary conditions [45]), a single-layer model (Lennard-Jones particles), and an analytically described solid boundary model (Lennard-Jones planes [13]). For the latter, the correction is excluded for fluid particles that have planes in their neighborhood.

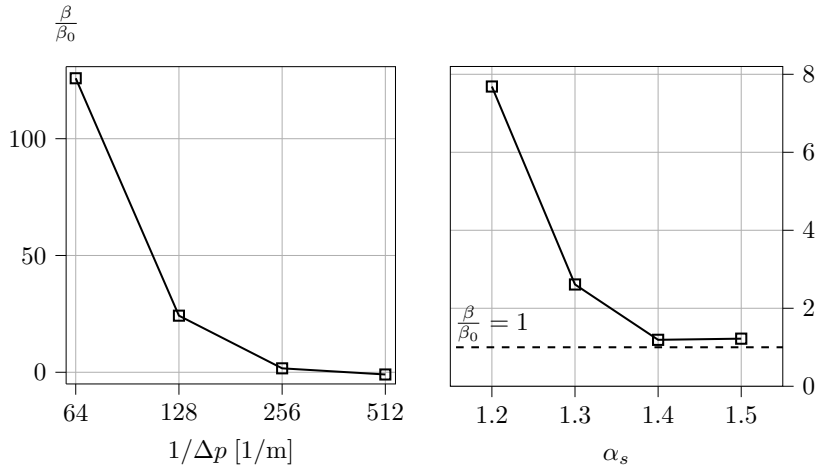

(a) Varying the particle spacing, Δp. The smoothing factor is fixed to $\alpha_s = 1.3$.

(b) Varying the smoothing factor, α_s. The spatial resolution is taken $\Delta p = 1/256$m.

Figure 9: Convergence test: trend of the quality index β/β_0.

5. Standing wave results for the improved formulation

Using the standing wave problem introduced in Section 3 we performed a convergence test with respect to the spatial resolution and the smoothing factor (Figure 9). In the case of changing Δp we use a fixed smoothing factor $\alpha_s = 1.3$. Figure 9a shows that the ratio β/β_0 approaches unity as the spatial resolution is refined, and thus, that the simulated results converge towards the analytical values.

It is worth observing that the ratio β/β_0 refers to the decay rates, and should not be directly interpreted as the error in the wave amplitude. We can consider as an example the value of $\beta/\beta_0 = 2.61$, obtained with a resolution of 256 particles per meter, indicating that the simulated wave decays with an equivalent viscosity of 2.61 times the physical viscosity. Considering the low value of the viscosity, the resulting decay is negligible in most of realistic time windows, as shown in Figure 10. Here, the deviation between the simulated and analytical amplitudes are comparable to the numerical precision.

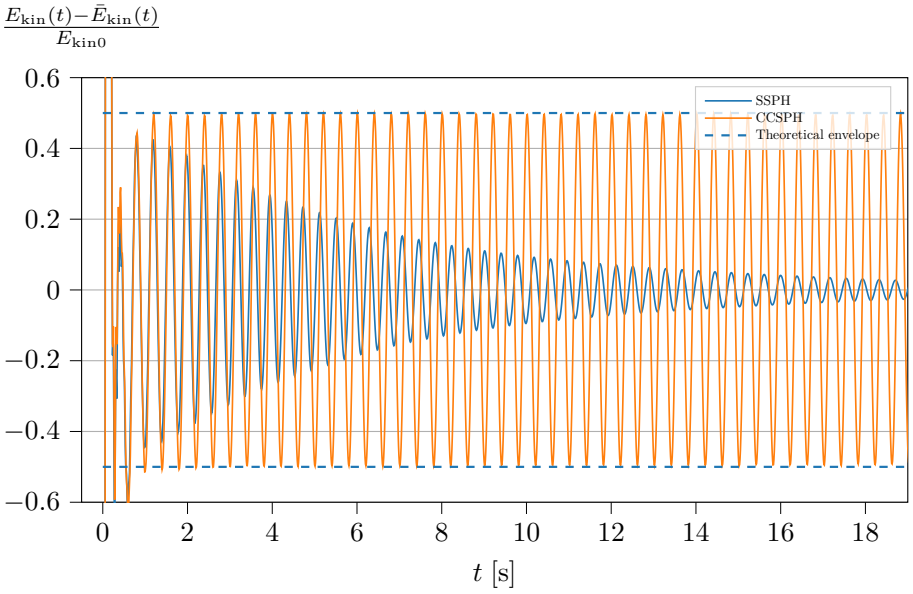

Figure 10: Comparison of kinetic energy for SSPH and CCSPH.

An irregularity in the convergence trend can be seen at a resolution of 512 particles per meter, where the β/β_0 ratio has a negative value of -0.947. This condition, that translates into a slow growth of the kinetic energy, is possibly due to the adoption of a non-Taylor-consistent gradient formulation [39] and limitations due to the machine precision [46]. However, the quality of the results shown in Figure 10 suggest that resolutions higher than 256 particles per meter are not needed. Therefore, the numerical issues arising for finer resolutions do not pose any problem to the applicability of the formulation.

Convergence is also obtained with respect to the smoothing factor, as shown in Figure 9b. Similarly to what was observed for varying the resolution, the convergence is impeded for values of α_s higher than 1.4. The same conclusions can be made here, as we saw that the amplitude decay obtained with 256 particles per meter, which uses a smoothing factor $\alpha_s = 1.3$, are negligible.

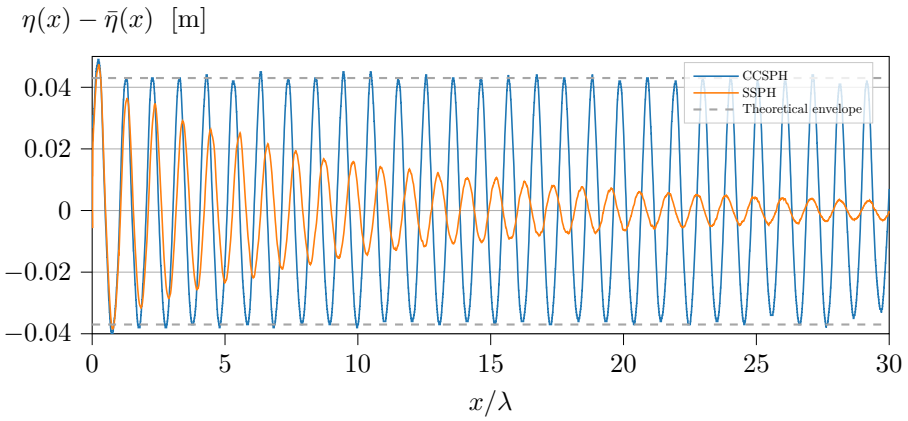

Figure 11: Water surface elevation in the NWT with respect to the mean water level. Results for SSPH and CCSPH are shown.

6. Improved progressive wave propagation

The progressive wave train problem introduced in Section 3 is now simulated with the new corrected formulation. Figure 11 shows the surface elevation along the wave tank for SSPH and for CCSPH. As discussed in Section 3, a de-trending has been performed also in this case. We set the wavelength to $\lambda = 1.5$m and simulate a distance corresponding to 30 wavelengths. A noticeable improvement in the maintenance of the wave amplitude is obtained with CCSPH. The theoretical amplitude decay, expected along the wavetank due to the viscosity of the fluid, can be predicted with Equation 13, and its value is around 0.1% (dashed lines in figure 11). This small decay is negligible in the simulation, as it is one order of magnitude below the discretization interval, Δp. The CCSPH formulation can successfully reproduce this result, as the waves reach the end of the tank without showing any apparent decay. On the other hand, the wave-train simulated with the SSPH formulation decays exponentially, dropping 92% of the nominal amplitude.

Some irregularities are present in the computed surface elevation that prevent it from being a perfect sinusoidal shape. These irregularities are appropriate for the simulated problem and are not related to the adopted formulation.

In particular, the larger waves in proximity of the tank origin are associated to the evanescent modes generated by the wavemaker [36]. The fluctuations in the amplitude and the offset are due to spurious waves in the tank, related to nonlinearities generated by the wavemaker and to the startup-related seiching phenomena. Finally, the distortion at the end of the tank is due to the interaction with the sloping region.

In addition to the benefits of the conservation of wave energy, the CCSPH improves the simulation of the wavelength. We estimate the wavelength of the simulated wave train by averaging over 15 periods. A length of 1.552m is obtained for the corrected formulation, against the nominal 1.5m, while it is 1.618m for standard SPH. We note that the nominal wavelength is obtained from the period of the wavemaker, using the dispersion relation, Equation 16, assuming linear wave theory.

7. Discussion on performance and quality of the simulations

As discussed in Section 4, kernel gradient corrections eliminate the excessive decay from SPH simulations similarly to approaches based on an increased smoothing factor, but with lower computational load. To make a quantitative assessment of the simulation performance, we simulated the standing wave problem using both approaches and the setup in Section 3. We take as reference a discretization interval of 256 particles per meter, that results in 532 480 particles, and a smoothing factor of $\alpha_s = 1.3$. The simulations are run on an NVIDIA Titan XP GPU. Using the SSPH formulation of Section 2, a time of 0.1s is simulated in 153s. If we adopt the kernel gradient correction, the required simulation time is 344s, while increasing the smoothing factor to $\alpha_s = 3.0$ brings the simulation time up to 1248s. In relative terms, using the kernel gradient correction increases the simulation time by a factor of 2.25, while using the larger smoothing factor results in a factor of 8.11. It is worth mentioning that $\alpha_s = 3.0$ is derived from Colagrossi *et al.* [3] as an indicative value for an acceptable energy conservation. In fact some spurious decay can be appreciated

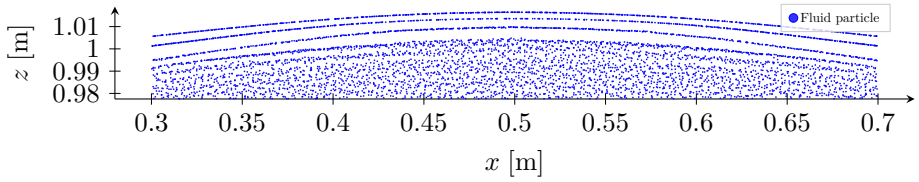

(a)

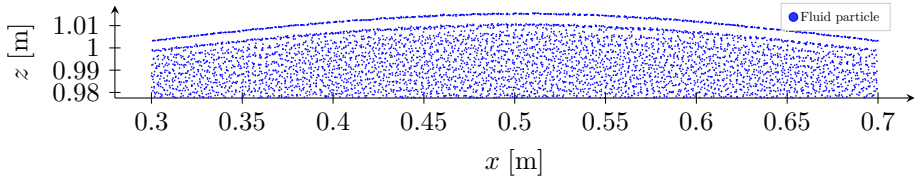

(b)

Figure 12: Particle distributions in the free-surface area at $t = 18.6$ s. (a): SSPH and $\alpha_s = 3.0$; (b): CCSPH and $\alpha_s = 1.3$.

on the kinetic energy, with $\beta/\beta_0 = 17.25$ (against the $\beta/\beta_0 = 2.61$ obtained using CCSPH and $\alpha_s = 1.3$).

7.1. Particle distribution

In addition to limiting simulation time, keeping a small smoothing factor helps reduce the amount of support incompleteness, as for example the layering occurring on free-surfaces. Large particle supports extend the layer of particles in proximity to the surface with incomplete support, resulting in the formation of multiple layering of particles below the free-surface. Figure 12 shows a comparison of the free-surface obtained with the two approaches. We can see that a smoothing factor of $\alpha_s = 3.0$ creates three layers of particles and a higher disorder of the underlying region. Figure 13 shows a close up of the free surface region during the three different phases of the standing wave and a close up of the domain bottom. For visual convenience the shown simulations are performed using $\Delta p = 1/128$. Because of the three-dimensional nature of the simulation the distribution of the particles cannot be directly appreciated, and visual artifacts resulting in striped regions also appear. However the images

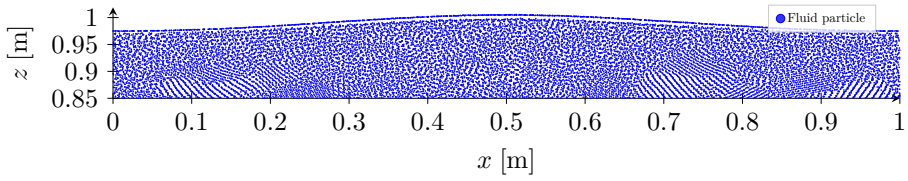

(a)

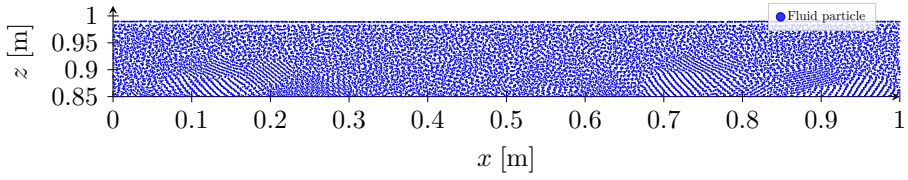

(b)

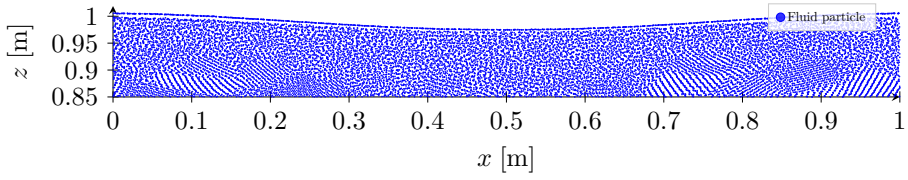

(c)

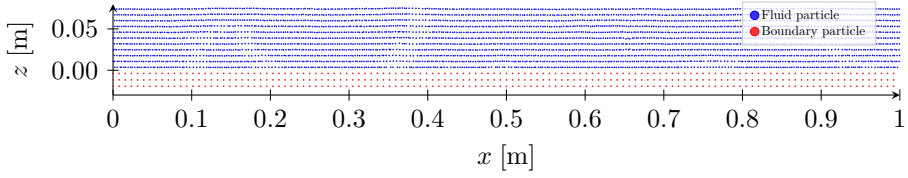

(d)

Figure 13: Particle distributions for the standing wave at the fifth oscillation. The free-surface area is shown for the three phases of the wave, and subfigure (d) shows the bottom of the domain.

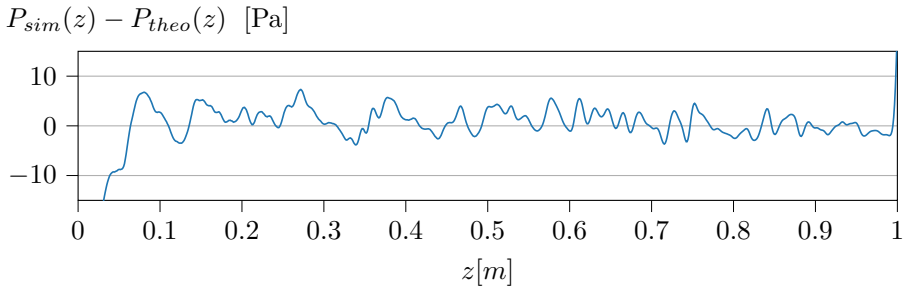

Figure 14: Pressure error for the standing wave at the beginning of the fifth oscillation. $z = 0$ corresponds to the bottom of the domain, while the data on the rightmost side of the plot correspond to the free surface.

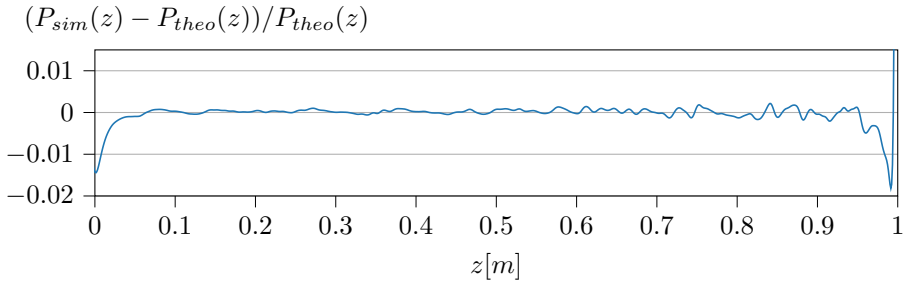

Figure 15: Relative pressure error for the standing wave at the beginning of the fifth oscillation. $z = 0$ corresponds to the bottom of the domain, while the data on the rightmost side of the plot correspond to the free surface.

can provide a reference for the quality of simulated free surface and fluid-solid interface.

7.2. Pressure field

Figure 14 shows the vertical profile of the pressure error for the standing wave at the beginning of the fifth oscillation, simulated with CCSPH, $\alpha_s = 1.3$ and 256 particles per meter. The simulated values are plotted as the SPH interpolation along a vertical line placed in the central region of the domain. At the considered instant, the surface of the domain is flat, therefore the theoretical pressure used for the computation of the error is equal to the hydrostatic pressure. The latter is computed considering the analytical free surface $\Delta p/2$

above the surface particles, so to take into account the particle's volume. The error increases in proximity of the bottom of the domain and the free surface, due to the truncation of the domain. Figure 15 shows the relative error, which is maintained below 0.5% of the theoretical value in most of the domain, and grows around 1.5% close to the domain discontinuities. In close proximity to the surface the relative error is not reliable, and the very large values are due to the theoretical pressure (used in the normalization) approaching zero.

8. Conclusions

An improved corrected SPH for wave propagation has been presented: CC-SPH. This scheme is able to substantially reduce excessive decay from simulated gravity waves when compared to standard SPH (SSPH), while maintaining low computational load and moderate implementation complexity.

The presented scheme works in 3D and solves the main issues that typically come with kernel gradient correction (KGC) techniques, such as the lack of momentum conservation and instabilities of the simulation. Thanks to the design of a reduced correction scheme (Section 4.2), our CCSPH avoids some volume conservation issues that appear for generic KGC when simulating very low viscosity fluids. The scheme is thus applicable to the simulation of water with realistic viscosity values, unlike many of the approaches mentioned in the introduction.

Throughout the paper we have characterized the amplitude decay for gravity waves and described how the simulations are affected. We presented our corrected formulation and addressed the criteria for the choice of the only parameter introduced by our scheme, $\det(A)_{th}$, which is a threshold on the determinant of the correction matrices.

We have then discussed some convergence tests, obtained for a standing wave, with respect to variations of the particle resolution and the smoothing factor. In both cases convergence has been assessed. Some irregularities were found in the convergence plots, but we saw that their onset occurs beyond values

of spatial discretization and smoothing factor for which the simulation errors are already negligible according to the numerical limits.

Finally, the simulation of a wave train in a long wave tank has been shown, where 30 wavelengths are simulated without exhibiting any excessive decay. This propagation distance is greater than that, to the best of our knowledge, is shown in the current literature. The limit of 30 wavelengths was only chosen in relation to the time required by the simulations, while the results that we have obtained don't suggest any limit on the propagation distance.

Improvements on the simulation of the wavelength and the free-surface were also shown. A final discussion about the simulation performance of the presented approach and an alternative proposed in the literature has been done.

Future developments of the proposed SPH scheme will address the optimization of the computational load, so as to reduce simulation times, and the possibility to free the scheme from the threshold on the matrices determinant, $\det(A)_{th}$.

9. Acknowledgments

A preliminary version of this work was presented at SPHERIC 2021 conference [47].

Funding

This research did not receive any specific grant from funding agencies in the public, commercial, or not-for-profit sectors.

References

[1] H. Gotoh, A. Khayyer, On the state-of-the-art of particle methods for coastal and ocean engineering, Coastal Engineering Journal 60 (2018) 79–103. doi:https://doi.org/10.1080/21664250.2018.1436243.

[2] H. Gotoh, A. Khayyer, Current achievements and future perspectives for projection-based particle methods with applications in ocean engineering, Journal of Ocean Engineering and Marine Energy 2 (2016) 251–278. doi:https://doi.org/10.1007/s40722-016-0049-3.

[3] A. Colagrossi, A. Souto-Iglesias, M. Antuono, S. Marrone, Smoothed-particle-hydrodynamics modeling of dissipation mechanisms in gravity waves, Physical review. E, Statistical, nonlinear, and soft matter physics 87 (2013) 023302. doi:10.1103/PhysRevE.87.023302.

[4] F. Macià, A. Colagrossi, M. Antuono, A. Souto-Iglesias, Benefits of using a Wendland kernel for free-surface flows, 6th ERCOFTAC SPHERIC Workshop on SPH Applications (2011) 30–37.

[5] M. Antuono, A. Colagrossi, S. Marrone, C. Lugni, Propagation of gravity waves through an SPH scheme with numerical diffusive terms, Computer Physics Communication 182 (4) (2011) 866–877. doi:10.1016/j.cpc.2010.12.012.

[6] P. M. Guilcher, G. Ducrozet, B. Alessandrini, P. Ferrand, Water Wave Propagation using SPH Models, 2nd SPHERIC workshop, January 2007, Madrid, Spain.

[7] Z. Wei, R. A. Dalrymple, A. Hérault, G. Bilotta, E. Rustico, H. Yeh, SPH modeling of dynamic impact of tsunami bore on bridge piers, Coastal Engineering 104 (2015) 26–42. doi:https://doi.org/10.1016/j.coastaleng.2015.06.008.
URL https://www.sciencedirect.com/science/article/pii/S0378383915001143

[8] Z. Wei, R. A. Dalrymple, R. Xu, R. Garnier, M. Derakhti, Short-crested waves in the surf zone, Journal of Geophysical Research 122 (2017) 4143–4162. doi:https://doi.org/10.1002/2016JC012485.

[9] Z. Wei, A. Hérault, G. Bilotta, E. Rustico, R. A. Dalrymple, SPH modeling of dynamic impact of tsunami bore on bridge piers, Coastal Engineering 105 (2015) 36–46.

[10] D. Zhang, Y. Shi, C. Huang, Y. Si, B. Huang, W. Li, SPH method with applications of oscillating wave surge converter, Ocean Engineering 152 (2018) 273 – 285. doi:https://doi.org/10.1016/j.oceaneng.2018.01.057.
URL http://www.sciencedirect.com/science/article/pii/S002980181830057X

[11] Y. You, A. Khayyer, X. Zheng, H. Gotoh, Q. Ma, Enhancement of δ-SPH for ocean engineering applications through incorporation of a background mesh scheme, Applied Ocean Research 110 (2021) 102508. doi:https://doi.org/10.1016/j.apor.2020.102508.
URL https://www.sciencedirect.com/science/article/pii/S0141118720310671

[12] R. Dalrymple, B. Rogers, Numerical modeling of water waves with the SPH wethod, Coastal Engineering 53 (2006) 141–147. doi:10.1016/j.coastaleng.2005.10.004.

[13] J. Monaghan, Simulating free surface flows with SPH, Journal of Computational Physics 110 (2) (1994) 399 – 406. doi:https://doi.org/10.1006/jcph.1994.1034.
URL http://www.sciencedirect.com/science/article/pii/S0021999184710345

[14] J. Chang, S.-X. Liu, J.-X. Li, A study of the stability properties in simulation of wave propagation with SPH method, China Ocean Engineering 31 (2) (2017) 173–182. doi:10.1007/s13344-017-0021-6.

[15] H. Wen, B. Ren, X. Yu, An improved SPH model for turbulent hydrodynamics of a 2d oscillating water chamber, Ocean Engineering 150 (2018) 152–166. doi:10.1016/j.oceaneng.2017.12.047.

[16] R. Gao, B. Ren, G. Wang, Y. Wang, Numerical modelling of regular wave slamming on subface of open-piled structures with the corrected SPH method, Applied Ocean Research 34 (2012) 173 – 186. doi:https://doi.org/10.1016/j.apor.2011.08.002.
URL http://www.sciencedirect.com/science/article/pii/S0141118711000630

[17] A. Trimuliono, H. Hashimoto, Experimental validation of Smoothed Particle Hydrodynamics on generation and propagation of water waves, Journal of Marine Science and Engineering 7 (17). doi:10.3390/jmse7010017.

[18] P. Omidvar, H. Norouzi, A. Zarghami, Smoothed Particle Hydrodynamics for water wave propagation in a channel, International Journal of Modern Physics 26 (08). doi:10.1142/S0129183115500850.

[19] M. Antuono, A. Colagrossi, The damping of viscous gravity waves, Wave Motion 50 (2) (2013) 197 – 209.

[20] S. Marrone, M. Antuono, A. Colagrossi, G. Colicchio, D. L. Touzé, G. Graziani, δ-SPH model for simulating violent impact flows, Computer Methods in Applied Mechanics and Engineering 200 (2011) 1526–1542. doi:10.1016/j.cma.2010.12.016.

[21] M. Antuono, A. Colagrossi, S. Marrone, Numerical diffusive terms in weakly-compressible SPH schemes, Computer Physics Communications 183 (12) (2012) 2570–2580. doi:https://doi.org/10.1016/j.cpc.2012.07.006.
URL https://www.sciencedirect.com/science/article/pii/S0010465512002342

[22] M. Antuono, S. Marrone, A. Colagrossi, B. Bouscasse, Energy balance in the δ-SPH´ scheme, Computer Methods in Applied Mechanics and Engineering 289 (2015) 209–226. doi:https://doi.org/10.1016/j.cma.2015.02.004.
URL https://www.sciencedirect.com/science/article/pii/S0045782515000456

[23] R. W. Randles, L. D. Libersky, Smoothed Particle Hydrodynamics: Some recent improvements and application, Computer Methods in Applied Mechanics Engineering 139 (1996) 375–408.

[24] G. R. Johnson, S. R. Beissel, Normalized smoothing functions for impact computations, International Journal of Numerical Methods and Engineering 39 (1996) 2725–2741.

[25] J. K. Chen, J. E. Beraun, C. J. Jih, An improvement for tensile instability in Smoothed Particle Hydrodynamics, Computational Mechanics 23 (4) (1999) 279–287. doi:10.1007/s004660050409.

[26] M. Liu, G. Liu, Smoothed Particle Hydrodynamics (SPH): an Overview and Recent Developments, Archives of Computational Methods in Engineering 17 (2010) 25–76. doi:10.1007/s11831-010-9040-7.

[27] Y. Xiao, X. Hong, Z. Tang, Normalized SPH without boundary deficiency and its application to transient solid mechanics, Meccanica, Springerdoi:10.1007/s11012-020-01255-6.

[28] J. J. Monaghan, Smoothed Particle Hydrodynamics, Reports on Progress in Physics 68 (2005) 1703–1759. doi:doi:10.1088/0034-4885/68/8/R01.

[29] H. Wendland, Piecewise polynomial, positive definite and compactly supported radial functions of minimal degree, Advances in Computational Mathematics 4 (1995) 389–396.

[30] V. Zago, G. Bilotta, A. Cappello, R. A. Dalrymple, L. Fortuna, G. Ganci, A. Hérault, C. Del Negro, Simulating complex fluids with Smoothed Par-

ticle Hydrodynamics, Annals of Geophysics 60 (6). doi:doi:10.4401/ag-7362.

[31] D. Molteni, A. Colagrossi, A simple procedure to improve the pressure evaluation in hydrodynamic context using the SPH, Computer Physics Communications 180 (2009) 861–872. doi:doi:10.1016/j.cpc.2008.12.004.

[32] M. Antuono, A. Colagrossi, S. Marrone, D. Molteni, Free-surface flows solved by means of SPH schemes with numerical diffusive terms, Computer Physics Communications 181 (3) (2010) 532–549. doi:https://doi.org/10.1016/j.cpc.2009.11.002.
URL https://www.sciencedirect.com/science/article/pii/S0010465509003506

[33] R. H. Cole, Underwater Explosion, (Princeton, NJ: Princeton University Press).

[34] A. Hérault, G. Bilotta, R. A. Dalrymple, SPH on GPU with CUDA, Journal of Hydraulic Research 48 (Extra Issue) (2010) 74–79.

[35] E. Saikali, G. Bilotta, A. Hérault, V. Zago, Accuracy improvements for single precision implementations of the SPH method, International Journal of Computational Fluid Dynamics 34 (10). doi:doi:10.1080/10618562.2020.1836357.

[36] R. G. Dean, R. A. Dalrymple, Water wave mechanics for engineers and scientists, World Scientific, 1991.

[37] A. Colagrossi, B. Bouscasse, S. Marrone, Energy-decomposition analysis for viscous free-surface flows, Phys. Rev. E 92 (2015) 053003. doi:10.1103/PhysRevE.92.053003.
URL https://link.aps.org/doi/10.1103/PhysRevE.92.053003

[38] Q. Zhu, L. Hernquist, Y. Li, Numerical convergence in Smoothed Particle Hydrodynamics, The Astrophysical Journal 800 (1). doi:doi:10.1088/0004-637X/800/1/6.

[39] G. Oger, M. Doring, B. Alessandrini, P. Ferrant, An improved SPH method: Towards higher order convergence, Journal of Computational Physics (2007) 1472–1492doi:10.1016/j.jcp.2007.01.039.

[40] A. Khayyer, H. Gotoh, S. Shao, Corrected incompressible SPH method for accurate water-surface tracking in breaking waves, Coastal Engineering 55 (3) (2008) 236–250. doi:https://doi.org/10.1016/j.coastaleng.2007.10.001.
URL https://www.sciencedirect.com/science/article/pii/S0378383907001172

[41] A. Khayyer, H. Gotoh, Y. Shimizu, K. Gotoh, On enhancement of energy conservation properties of projection-based particle methods, European Journal of Mechanics - B/Fluids 66 (2017) 20–37. doi:https://doi.org/10.1016/j.euromechflu.2017.01.014.
URL https://www.sciencedirect.com/science/article/pii/S0997754616302175

[42] A. Mayrhofer, B. D. Rogers, D. Violeau, M. Ferrand, Investigation of wall bounded flows using SPH and the unified semi-analytical wall boundary conditions, Computer Physics Communications 184 (11) (2013) 2515–2527. doi:https://doi.org/10.1016/j.cpc.2013.07.004.
URL https://www.sciencedirect.com/science/article/pii/S0010465513002324

[43] J. J. Monaghan, Smoothed Particle Hydrodynamics, Annual Review of Astronomy and Astrophysics 30 (1992) 543–574. doi:10.1146/annurev.aa.30.090192.002551.

[44] J. P. Vila, On particle weighted methods and Smooth Particle Hydrodynamics, Mathematical Models and Methods in Applied Sciences 9 (2). doi:10.1142/S0218202599000117.

[45] A. A. J. C. Crespo, M. Gomez-Gesteira, R. A. Dalrymple, Boundary condi-

tions generated by dynamic particles in SPH methods, Computers, Materials and Continua 5 (2007) 173–184. doi:10.1103/PhysRevE.92.053003.

[46] B. Schrader, S. Reboux, I. F. Sbalzarini, Discretization correction of general integral PSE Operators for particle methods, Journal of Computational Physics 229 (11). doi:doi:10.1016/j.jcp.2010.02.004.

[47] V. Zago, L. J. Schulze, G. Bilotta, N. Almashan, R. A. Dalrymple, A conservative corrective SPH for water wave propagation, 2021 International SPHERIC Workshop, Virtual Meeting, June 7-11, 2021.

Appendix A. Kernel gradient correction

We derive here the standard kernel gradient correction formulation, following the approach of Oger *et al.* [39]. For simplicity, we will refer to the 2D case, and the final results will be extended to the 3D case. Let us consider the equation $\nabla f = \frac{1}{\phi}\left(\nabla\left(\phi f\right) - f\nabla\phi\right)$. For $\phi = 1$ this yields

$$\nabla f = \nabla f - f\nabla 1. \tag{A.1}$$

If the SPH approximation of a gradient of a function is considered in its continuous form and inserted in the right hand side,

$$\nabla f\left(\mathbf{x}\right) \approx \int_{\Omega} f\left(\mathbf{x}'\right)\nabla W \mathrm{d}\mathbf{x}' - f\left(\mathbf{x}\right)\int_{\Omega}\nabla W \mathrm{d}\mathbf{x}' \tag{A.2}$$

is obtained, in which the abbreviation $\nabla W = \nabla W\left(|\mathbf{x} - \mathbf{x}'|, h\right)$ is adopted. The Taylor expansion for the first term on the right hand side about $\mathbf{x} = x\mathbf{e}_1 + y\mathbf{e}_2$ yields

$$\begin{aligned}\int_{\Omega} f\left(\mathbf{x}'\right)\nabla W \mathrm{d}\mathbf{x}' = f\left(\mathbf{x}\right)\int_{\Omega}\nabla W \mathrm{d}\mathbf{x}' + \frac{\partial f\left(\mathbf{x}\right)}{\partial x}\int_{\Omega}\left(x' - x\right)\nabla W \mathrm{d}\mathbf{x}' \\ + \frac{\partial f\left(\mathbf{x}\right)}{\partial y}\int_{\Omega}\left(y' - y\right)\nabla W \mathrm{d}\mathbf{x}' + \mathcal{O}\left(h^2\right).\end{aligned} \tag{A.3}$$

If the Taylor expansion is inserted in Eq. (A.2), the first term of the expansion and the second term on the right hand side of Eq. (A.2) cancel each other, such that the SPH approximation of the gradient of f yields

$$\nabla f\left(\mathbf{x}\right) \approx \frac{\partial f\left(\mathbf{x}\right)}{\partial x}\underbrace{\int_{\Omega}\left(x' - x\right)\nabla W \mathrm{d}\mathbf{x}'}_{\mathrm{A}} + \frac{\partial f\left(\mathbf{x}\right)}{\partial y}\underbrace{\int_{\Omega}\left(y' - y\right)\nabla W \mathrm{d}\mathbf{x}'}_{\mathrm{B}}. \tag{A.4}$$

Here, the terms depending on h to the power of two or higher originating from the Taylor expansion have been omitted and can also be viewed as a contribution towards the approximation error.

It is straightforward to identify desired values of the integral terms. In order to provide particularly well-posed approximations of gradients, A and B have to yield $\mathbf{e}_1$ and $\mathbf{e}_2$, respectively. If the integrals are approximated as the sum

over a finite set of particles, and a cartesian coordinate system is assumed, the conditions result in

$$\begin{aligned} \sum_j (x_j - x_i) \nabla W_{ij} V_j &= \begin{pmatrix} 1 \\ 0 \end{pmatrix}, \\ \sum_j (y_j - y_i) \nabla W_{ij} V_j &= \begin{pmatrix} 0 \\ 1 \end{pmatrix}. \end{aligned} \tag{A.5}$$

If the kernel gradient is unaltered, these conditions do not necessarily hold. For this reason, a linear mapping is constructed, that is applied to the kernel gradients and corrects them in the sense that they satisfy Equation (A.5). A corrected kernel gradient can therefore be obtained by applying a corrective matrix associated with particle i, as described in Equation 20. In order to identify how $\mathbf{B}_i$ can be constructed, so that $\tilde{\nabla} W_{ij}$ fulfills Equation (A.5), the conditions are written in matrix-vector notation, and using Equation 20 we have:

$$\sum_j \left((\mathbf{x}_j - \mathbf{x}_i) V_j \nabla W_{ij}^{\mathrm{T}} \right) \mathbf{B}_i^{\mathrm{T}} = \begin{pmatrix} 1 & 0 \\ 0 & 1 \end{pmatrix}. \tag{A.6}$$

It is now straightforward to determine $\mathbf{B}_i$, namely

$$\mathbf{B}_i = \begin{pmatrix} \sum_j (x_j - x_i) \frac{\partial W_{ij}}{\partial x} V_j & \sum_j (y_j - y_i) \frac{\partial W_{ij}}{\partial x} V_j \\ \sum_j (x_j - x_i) \frac{\partial W_{ij}}{\partial y} V_j & \sum_j (y_j - y_i) \frac{\partial W_{ij}}{\partial y} V_j \end{pmatrix}^{-1} = \mathbf{A}_i^{-1}. \tag{A.7}$$

Extending this matrix to the 3D case, we obtain Equation 19.